



Cite this: *Phys. Chem. Chem. Phys.*,  
2016, **18**, 32744

# Na<sub>2</sub>CoSiO<sub>4</sub> as a cathode material for sodium-ion batteries: structure, electrochemistry and diffusion pathways†

Joshua C. Treacher,<sup>a</sup> Stephen M. Wood,<sup>b</sup> M. Saiful Islam<sup>\*b</sup> and Emma Kendrick<sup>\*ac</sup>

The importance of developing new low-cost and safe cathodes for large-scale sodium batteries has led to recent interest in silicate compounds. A novel cobalt orthosilicate, Na<sub>2</sub>CoSiO<sub>4</sub>, shows promise as a high voltage (3.3 V vs. Na/Na<sup>+</sup>) cathode material for sodium-ion batteries. Here, the synthesis and room temperature electrochemical performance of Na<sub>2</sub>CoSiO<sub>4</sub> have been investigated with the compound found to yield a reversible capacity greater than 100 mA h g<sup>-1</sup> at a rate of 5 mA g<sup>-1</sup>. Insights into the crystal structures of Na<sub>2</sub>CoSiO<sub>4</sub> were obtained through refinement of structural models for its two polymorphs, *Pn* and *Pbca*. Atomistic modelling results indicate that intrinsic defect levels are not significant and that Na<sup>+</sup> diffusion follows 3D pathways with low activation barriers, which suggest favourable electrode kinetics. The new findings presented here provide a platform on which future optimisation of Na<sub>2</sub>CoSiO<sub>4</sub> as a cathode for Na-ion batteries can be based.

Received 3rd October 2016,  
Accepted 14th November 2016

DOI: 10.1039/c6cp06777h

www.rsc.org/pccp

## 1. Introduction

Sodium-ion batteries are currently attracting widespread attention for grid-level energy storage applications due to the low cost and widespread abundance of sodium compared to lithium.<sup>1–4</sup> Developing new cheap and safe cathode materials is a key target for large-scale sodium-ion batteries.<sup>5</sup>

Many different sodium-based cathode materials have been investigated to date.<sup>2,3,6,7</sup> Polyanionic compounds, with robust and stable frameworks, have garnered recent interest as potential cathodes and include NaFePO<sub>4</sub>, Na<sub>2</sub>FePO<sub>4</sub>F and Na<sub>3</sub>V<sub>2</sub>(PO<sub>4</sub>)<sub>3</sub>.<sup>2,8,9</sup> Transition metal silicates, in particular, offer the potential for low-cost cathodes due to the high abundance of silicon in the earth's crust. As such, lithium-based silicates, Li<sub>2</sub>MSiO<sub>4</sub> (M = Mn, Co or Fe), have been investigated extensively.<sup>8,10–16</sup> These orthosilicate materials are of particular interest due to the possibility of two-electron redox processes and hence higher capacities. Li<sub>2</sub>MSiO<sub>4</sub> compounds belong to a family of tetrahedral oxide structures that consist of slightly distorted close-packed oxygen layers in between which cations occupy half of the tetrahedral sites. The cations can order within the tetrahedral sites in different ways, leading to a rich polymorphism, as described previously.<sup>11</sup>

In contrast to lithium silicate cathodes, there are limited structural and electrochemical studies of the sodium silicate analogues, Na<sub>2</sub>MSiO<sub>4</sub> (M = Mn, Co or Fe).<sup>17–22</sup> Chen *et al.* report a reversible capacity of 125 mA h g<sup>-1</sup> at a rate of C/10 for Na<sub>2</sub>MnSiO<sub>4</sub> using an ionic liquid electrolyte at elevated temperatures.<sup>18</sup> In many of these cases, the as-prepared compounds possess small impurity peaks, as is often found for the lithium silicates, highlighting the difficult synthesis of these types of materials. Recently, Kee *et al.*<sup>20</sup> synthesised Na<sub>2</sub>FeSiO<sub>4</sub> in an impure form (~85%) with Na<sub>2</sub>SiO<sub>3</sub> as the major impurity. They report a specific capacity of 126 mA h g<sup>-1</sup> at an average voltage of 1.7 V vs. Na/Na<sup>+</sup> at low rates of C/40. Diffusion studies have been performed using *ab initio* calculations for *Pn* structured Na<sub>x</sub>Li<sub>2-x</sub>MnSiO<sub>4</sub> (x = 2, 1 or 0) and they suggest 3D diffusion pathways.<sup>19</sup> Na<sub>2</sub>CoSiO<sub>4</sub> has a theoretical specific capacity of 272.06 mA h g<sup>-1</sup> for a two electron process. All reported observed specific capacities for sodium orthosilicates are for a one electron process.

Here we have studied the physical properties of the sodium transition metal orthosilicates, and have looked in particular at the cobalt systems. It is apparent that the structural, electrochemical and sodium ion transport properties of the Co-based compound Na<sub>2</sub>CoSiO<sub>4</sub> have not been established. We report for the first time two distinct polymorphs of the transition metal orthosilicate, Na<sub>2</sub>CoSiO<sub>4</sub>, with similar compositions, synthesised using different methods. We recognise that cobalt is not a transition metal of choice for sodium ion batteries because of the high cobalt price. Nevertheless, Na<sub>2</sub>CoSiO<sub>4</sub> is stable in air unlike many other sodium ion cathode materials,<sup>23</sup> and gives

<sup>a</sup> Sharp Laboratories of Europe Ltd., Oxford Science Park, Oxford, OX4 4GB, UK.

E-mail: emma.kendrick@sharp.co.uk

<sup>b</sup> Department of Chemistry, University of Bath, Bath, BA2 7AY, UK.

E-mail: m.s.islam@bath.ac.uk

<sup>c</sup> School of Chemistry, University of Birmingham, Birmingham, B15 2TT, UK

† Electronic supplementary information (ESI) available. See DOI: 10.1039/c6cp06777h

the added benefit of being able to perform ink mixes and electrode coatings in standard conditions outside of a dry room. Whilst lithium iron silicates have the potential for low cost cathode materials for lithium ion batteries, sodium iron silicate cathode batteries would offer an even lower cost solution, and this is due to the high availability of the iron, silicon and sodium in the earth crust. However the operating voltage for the sodium iron silicate is low (1.9 V vs. Na/Na<sup>+</sup>) and therefore the material has a low energy density and is extremely water sensitive which limits its usefulness as a battery cathode material. The cobalt systems have a surprisingly high voltage (3.3 V vs. Na/Na<sup>+</sup>) compared to the iron systems. The fundamental understanding gained from this work can also be utilised to further improve the electrochemical properties of other sodium orthosilicate materials.

Here, we report the electrochemical performance and crystal structure of Na<sub>2</sub>CoSiO<sub>4</sub> synthesised using co-precipitation and solid-state techniques. In addition, we present the first atomic-scale insights into the defect chemistry and Na<sup>+</sup> diffusion pathways using atomistic simulation methods.

## 2. Experimental

### 2.1. Synthesis and characterisation

Na<sub>2</sub>CoSiO<sub>4</sub> was synthesised using both co-precipitation and solid-state synthesis routes. For the co-precipitation route, 0.03 mol CoCl<sub>2</sub> (Sigma, anhydrous) was dissolved in deionised water (10 mL) to which 0.03 mol tetraethylorthosilicate (Sigma) and ethanol (5 mL) were added. The mixture underwent a nitric acid catalysed condensation for 1 h before a base catalysation with 8 M sodium hydroxide (15 mL). Base catalysation resulted in a gel which was subsequently dried overnight at 120 °C under vacuum. Sodium chloride was removed from the dried gel by an ethylene glycol rinse either prior or subsequently to heat treatment. A final heat treatment was performed under nitrogen for 8 h at temperatures between 500 and 900 °C.

For the solid-state method, 0.03 mol Na<sub>2</sub>SiO<sub>3</sub> (Sigma, anhydrous >97%) and 0.03 mol CoCO<sub>3</sub> (Sigma) were milled in a Retch™ PM 100 planetary ball mill for 30 min at 400 rpm with acetone (25 mL). This precursor mix was dried at a temperature of 120 °C under vacuum before a subsequent heat treatment at 800 °C for 8 h under flowing nitrogen. X-ray diffraction (XRD) was performed on all samples using a Bruker D2 phaser with a Cu Kα<sub>1</sub> and Kα<sub>2</sub> source or Co Kα<sub>1</sub> and Kα<sub>2</sub> source. Scans were performed at 0.02° 2θ steps from 10 to 90° 2θ over 13 h. Rietveld refinements were performed on high-quality diffraction data using the general system analysis system (GSAS) suite of programmes.<sup>24</sup> Scanning electron microscopy (SEM) was performed using a Hitachi UHR-SEM SU-70 with an acceleration voltage of 10 kV. Particle size was estimated from the SEM images using the ImageJ software package.<sup>25</sup>

Energy dispersive X-ray (EDX) analysis was conducted using the aforementioned SEM in combination with an Oxford Instruments X-max<sup>N</sup> 80 EDX detector at 10 kV acceleration voltage. The sample Na<sub>2</sub>CoSiO<sub>4</sub> was prepared as an electrode (details in Section 2.2)

with this then hot calendared at 120 °C at maximum pressure to produce a flat surface. Four sites were then picked at random and the compositional ratio was recorded based upon an average.

### 2.2. Electrochemistry

Na<sub>2</sub>CoSiO<sub>4</sub> materials were tested in two electrode Swagelok™ type cells using a Maccor Series 4000. Inks of the orthosilicate, carbon black (C65 Timcal) and PVDF binder (8:2:1) in NMP were cast onto a carbon coated aluminium current collector and dried at 120 °C under vacuum to remove the solvent. Cathode loadings were approximately 6 mg cm<sup>-2</sup>. The cells were constructed with two glass fibre GF/A Whatman disks used as a separator, a sodium metal counter electrode and 0.5 M NaClO<sub>4</sub> in propylene carbonate (PC) was used as the electrolyte. Galvanostatic electrochemical testing was performed at room temperature between the voltages of 3.75 and 1.5 V vs. Na/Na<sup>+</sup> at a current of 5 mA g<sup>-1</sup> which is C/20 assuming a specific capacity of 100 mA h g<sup>-1</sup>. Rate testing has not been performed as part of this study. The kinetics have been improved in the lithium orthosilicates through testing at higher temperatures, carbon coatings and nano-sizing. It is assumed that the kinetics for the sodium ion orthosilicates can be improved using the same techniques and improvement in the electrode formulations, which is not the focus of this study.

### 2.3. Simulation methods

Atomistic modelling techniques have been widely used in the study of defect and transport properties of solids, and are detailed elsewhere.<sup>26–28</sup> Interatomic interactions were represented by a long-range electrostatic term plus a function representing the short-range repulsive and van der Waals interactions. A crucial feature of defect simulations is the treatment of lattice relaxation about the charged defect or migrating Na<sup>+</sup> ion. The Mott–Littleton approach was used, whereby the crystal lattice is partitioned into two regions, implemented in the GULP code.<sup>29</sup> This approach has previously been used effectively to explore a number of battery materials.<sup>26,30–35</sup> Large-scale molecular dynamics (MD) simulations were performed with LAMMPS<sup>36</sup> using the potential model of Pedone *et al.*,<sup>37</sup> which has been developed to allow rapid MD simulations of complex oxides. A supercell consisting of ~11 000 ions was used, with 10% of Na ions removed randomly. The systems were equilibrated for at least 1 ns (with a time step of 2.0 fs) before the main simulation runs of ~8 ns were performed. It should be noted that current *ab initio* MD simulations on battery cathode materials are of the order of only 20 ps. An *NPT* ensemble, with a Berendsen thermostat, was used throughout to allow for thermal expansion. Such potentials-based MD techniques have previously been applied successfully to a wide range of materials for lithium batteries and solid oxide fuel cell ion conductors.<sup>26,38–43</sup>

## 3. Results and discussion

### 3.1. Structures of Na<sub>2</sub>CoSiO<sub>4</sub>

Na<sub>2</sub>CoSiO<sub>4</sub> was synthesised successfully by solid-state and co-precipitation techniques. The solid-state method produced

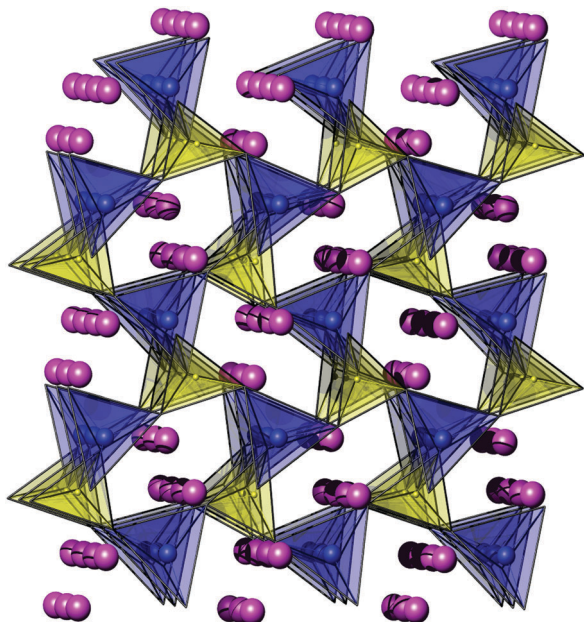


Fig. 1 Crystal structure of the ordered monoclinic  $\text{Na}_2\text{CoSiO}_4$  phase synthesised via the co-precipitation method. Pink spheres are sodium sites, blue tetrahedra are  $\text{CoO}_4$  units and yellow tetrahedra are  $\text{SiO}_4$  units.

a highly crystalline  $\text{Na}_2\text{CoSiO}_4$  phase which could be fitted to a monoclinic ( $Pn$ ) space group, as observed previously for  $\text{Na}_2\text{MgSiO}_4$ <sup>44</sup> and  $\text{Na}_2\text{ZnSiO}_4$ .<sup>45</sup> The structure can be considered as a ‘stuffed’ cristobalite with corner sharing alternate transition metal and silicate tetrahedral units, taking the place of the solely silicate units observed in pure cristobalite, with sodium atoms stuffed onto the tetrahedral vacant sites. The silicon and cobalt atoms are in distinct crystallographic sites within the unit cell. A schematic of this monoclinic structure illustrating the alternating silicate and cobalt tetrahedral framework is shown in Fig. 1.

An orthorhombic structure with a  $Pn2_1a$  space group was also considered. However, a better fit was obtained with the monoclinic unit cell and therefore this model was used for the Rietveld refinements and simulations. The monoclinic model gave the following fit parameters and lattice parameters;  $wR_p - 0.0349$ ,  $R_p - 0.0250$ ,  $X^2 - 2.231$ ,  $a = 7.0355(3)$  Å;  $b = 10.9552(4)$  Å;  $c = 5.2509(2)$  Å;  $\beta = 89.954(9)^\circ$ . A comparison of the two Rietveld refinements can be seen in ESI,<sup>†</sup> data S1.

Alternatively,  $\text{Na}_2\text{CoSiO}_4$  can be formed through the described co-precipitation method. The initial co-precipitation creates only a partially ordered  $\text{Na}_2\text{CoSiO}_4$  phase alongside a crystalline sodium chloride by-product. Subsequent heat treatment of the materials was performed under flowing nitrogen at temperatures of 500, 700 or 900 °C with the sodium chloride removed via a wash in ethylene glycol either before or after the firing stage.

After the successful synthesis of  $\text{Na}_2\text{CoSiO}_4$ , structural and electrochemical investigations were performed. The crystallinity of the product was observed to increase with the higher temperature heat treatments, as can be observed in Fig. 2 and 3. Fig. 2 shows the XRD patterns for the material where NaCl is removed before annealing. A single peak can be seen at approximately

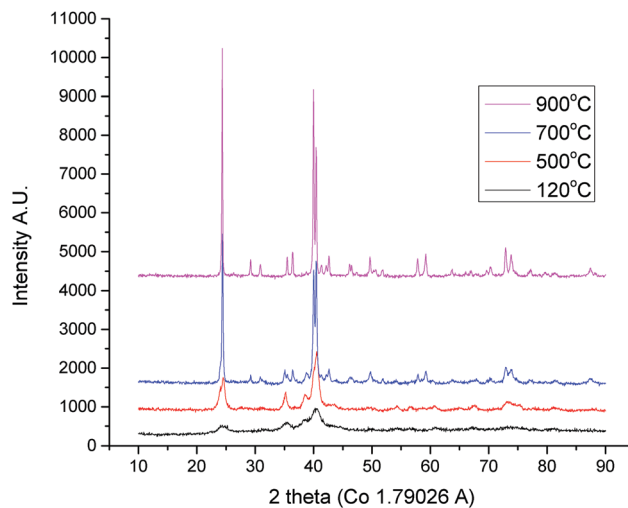


Fig. 2 X-ray diffraction patterns of  $\text{Na}_2\text{CoSiO}_4$  made by the co-precipitation method with NaCl removed before annealing.

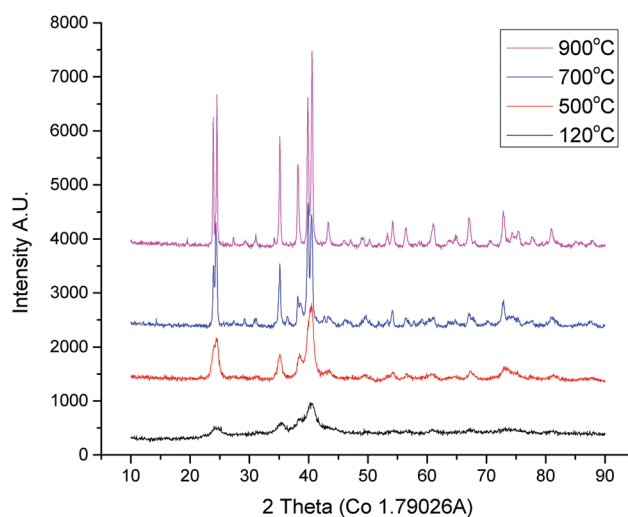


Fig. 3 X-ray diffraction patterns of  $\text{Na}_2\text{CoSiO}_4$  made by the co-precipitation method with NaCl removed after annealing.

$2\theta = 24^\circ$ . Fig. 3 shows the XRD patterns of the materials annealed with the NaCl flux agent; two peaks are observed at approximately  $2\theta = 24^\circ$ . The XRD pattern of the washed precipitate (black) is given in both diagrams for comparison to the annealed phases. The materials produced by the co-precipitation method contained no or very low levels of impurities compared to the solid-state synthesis. Elemental analysis by EDX of calendared coatings confirmed  $2(0.1)\text{Na}:1(0.05)\text{Co}:1(0.05)\text{Si}$  molar ratio with low errors.

When the precipitate is heat-treated with the NaCl flux agent, a material that is isostructural with  $\text{Na}_2\text{CoSiO}_4$  made by the solid-state method is observed. Rietveld refinement of the 900 °C phase was performed with the XRD data collected with a cobalt X-ray source, which reduced the background bremsstrahlung radiation observed compared to a copper X-ray source. A good fit to the monoclinic structure was observed

**Table 1** Summary of the Rietveld refinement data for  $\text{Na}_2\text{CoSiO}_4$  made by the solid-state and co-precipitation methods. Average bond lengths can be seen in S4 (ESI)

	Solid-state	Co-precipitation + NaCl	Co-precipitation
Firing temperature ( $^\circ\text{C}$ )	800	900	900
Space group	<i>Pn</i> Monoclinic	<i>Pn</i> Monoclinic	<i>Pbca</i> Orthorhombic
Lattice parameters			
<i>a</i> ( $\text{\AA}$ )	7.0355(3)	7.0433(2)	10.4543(3)
<i>b</i> ( $\text{\AA}$ )	10.9552(4)	10.9128(4)	14.4724(3)
<i>c</i> ( $\text{\AA}$ )	5.2509(2)	5.2396(2)	5.2274(2)
$\beta$ ( $^\circ$ )	89.954(9)	90.02(1)	90.0(0)
Vol.	404.717(28)	402.73(3)	790.90(4)

with lattice parameters of  $a = 7.0433(2) \text{ \AA}$ ,  $b = 10.9128(4) \text{ \AA}$ ,  $c = 5.2396(2) \text{ \AA}$  and  $\beta = 90.02(1)^\circ$  ( $wR_p - 0.0388$ ,  $R_p - 0.0274$ ,  $\chi^2 10.6$  (S2, ESI<sup>†</sup>)).

The removal of sodium chloride before annealing resulted in  $\text{Na}_2\text{CoSiO}_4$  materials that exhibited lower ordering of the cobalt and silicon tetrahedral units. A similar tetrahedral  $\beta\text{-NaFeO}_2$  phase or cristobalite type structure type is observed, but cobalt and silicon share the same crystallographic site, rather than occupying distinct sites. In particular, the observed reflection at  $24^\circ 2\theta$  is a singlet rather than the doublet observed for the monoclinic phase. Rietveld refinement was again performed on the sample annealed at  $900^\circ\text{C}$  and the fit can be observed in S3 (ESI<sup>†</sup>). This crystal structure has an orthorhombic *Pbca* space group with corner-sharing cobalt and silicon tetrahedra, and sodium tetrahedra corner sharing with both the silicon and cobalt. However, a much more disordered structure is observed. In addition to the shared crystallographic positions for the cobalt and silicon tetrahedra, the sodium is also more disordered throughout the structure partially four different atomic positions. The orthorhombic model gave the following fit parameters and lattice parameters:  $wR_p - 0.0372$ ,  $R_p - 0.0266$ ,  $\chi^2 - 10.51$ ;  $a = 10.4543(3) \text{ \AA}$ ,  $b = 14.4724(3) \text{ \AA}$ ,  $c = 5.2274(2) \text{ \AA}$ . A summary of the different crystal structures and their average bond lengths can be seen in Table 1. The atomic positions can be seen in S1–S3 (ESI<sup>†</sup>).

Low levels of residual carbon are observed in these materials when synthesised *via* the coprecipitation method (S12b, ESI<sup>†</sup>), as measured by CHN analysis. 0.75 wt% after annealing at  $500^\circ\text{C}$ , and 0.28 wt% and 0.45 wt% after annealing at  $700^\circ\text{C}$  with NaCl removed before and after firing respectively. Excess carbon during the synthesis has been shown to result in partial carbothermal reduction to cobalt metal. An example of this can be observed in ESI<sup>†</sup>, S12a. The synthesis processes presented here have thus been optimised to avoid the reduction of cobalt(II) and lead to the production of high purity orthosilicate materials.

### 3.2. Electrochemical studies

Lithium orthosilicates made by sol-gel and co-precipitation methods have been reported previously.<sup>46</sup> These high purity materials possess small particle sizes and exhibit improved

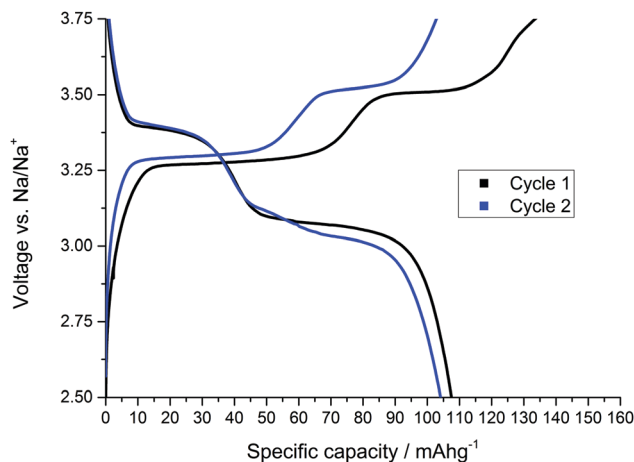


**Fig. 4** Voltage vs. specific capacity plot for  $\text{Na}_2\text{CoSiO}_4$  synthesised *via* the solid-state method.

electrochemical performances due to the shorter lithium-ion diffusion pathways. In contrast, lithium transition metal silicates synthesised by the solid-state method exhibit lower capacities and poor cycle life.<sup>46</sup>  $\text{Na}_2\text{CoSiO}_4$  has been investigated to determine whether similar trends are observed.

The sample of  $\text{Na}_2\text{CoSiO}_4$  made *via* the solid-state method was found to be electrochemically active (Fig. 4). A first discharge capacity of  $107 \text{ mA h g}^{-1}$  was observed and the average voltage on discharge on the second cycle was 3.29 V, although the hysteresis was found to increase rapidly upon cycling, hindering any longer-term cycling. SEM images (S5, ESI<sup>†</sup>) show a large variance in primary particle size from approximately 0.5 to  $20 \mu\text{m}$ , which is likely to contribute to the large hysteresis.

Electrochemical studies were conducted on both the as-made precipitate dried at  $120^\circ\text{C}$  and the subsequently annealed samples ( $500$ ,  $700$  and  $900^\circ\text{C}$ ). The electrochemical consequences of the presence of the NaCl flux-agent during the anneal were also examined. In all cases, the materials were electrochemically active and exhibited reversible sodium deintercalation and intercalation.

The as-made, washed and dried precipitate was electrochemically tested *vs.* a sodium metal anode. A sloping voltage profile was observed from 1.5 to 3.75 V *vs.*  $\text{Na}/\text{Na}^+$  and an initial specific discharge capacity of  $125 \text{ mA h g}^{-1}$  was observed. However, due to the poor crystallinity and high surface area of this material, a significant loss of greater than 50% was observed in the first cycle and the fade rate was subsequently high (see S6, ESI<sup>†</sup>).

As observed from the X-ray diffraction studies, higher temperature heat treatments gave rise to higher crystallinity materials, even at an annealing temperature of  $500^\circ\text{C}$ . The low annealing temperature of  $500^\circ\text{C}$  gave specific capacities of approximately  $90 \text{ mA h g}^{-1}$  on first discharge for both samples which were annealed with and without NaCl, and both have a high first cycle loss of approximately 40% (see S7, ESI<sup>†</sup>). The voltage profile for the  $500^\circ\text{C}$  materials show two distinct reversible voltage plateaus which relate to the two cobalt sites present in both the monoclinic and orthorhombic structured material.

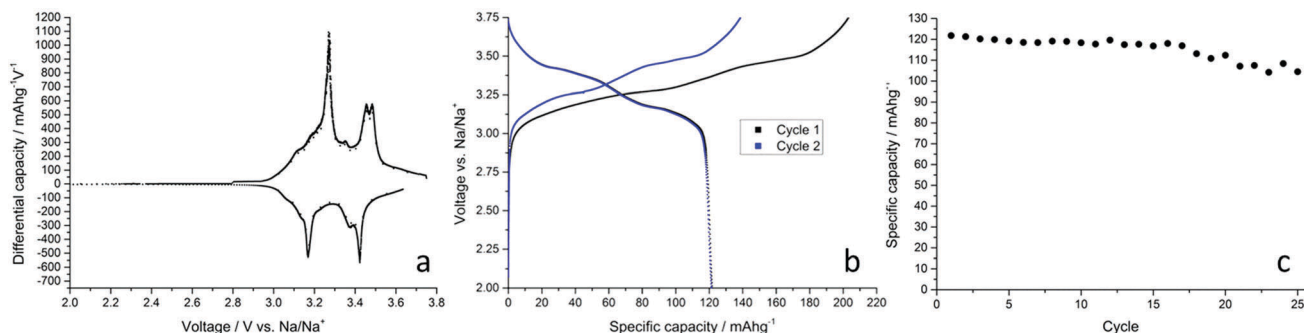


Fig. 5 Differential capacity vs. voltage plot (left, first cycle only), voltage vs. specific capacity plot (centre) and specific discharge capacity vs. cycle number (right) for first two cycles of  $\text{Na}_2\text{CoSiO}_4$  synthesised at  $700^\circ\text{C}$  with NaCl removed before the anneal.

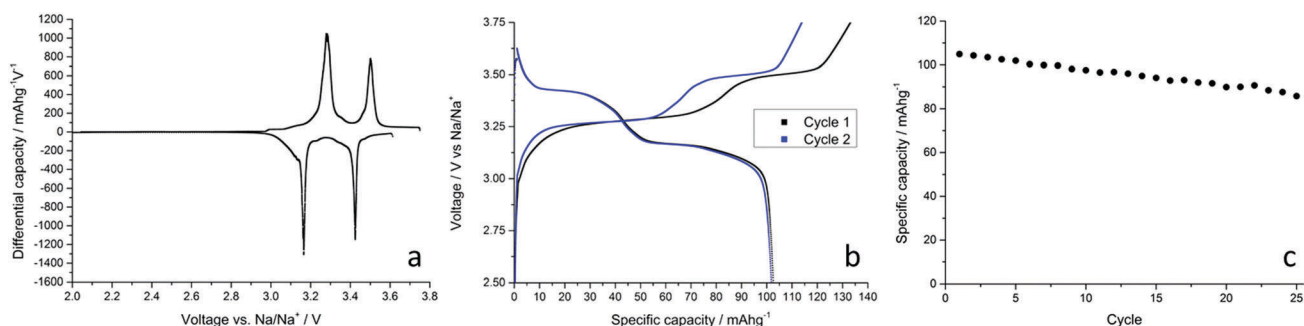


Fig. 6 Specific discharge capacity vs. cycle number (right) for first two cycles of  $\text{Na}_2\text{CoSiO}_4$  synthesised at  $700^\circ\text{C}$  with NaCl present during the anneal.

This is in contrast to the sample that was simply dried at  $120^\circ\text{C}$  which shows more solid solution type behaviour, as observed by the sloping voltage profiles (S6, ESI†).

The differential capacity plots, voltage profiles and capacity vs. cycle number plots for the materials annealed at  $700^\circ\text{C}$  are shown in Fig. 5 and 6 ( $900^\circ\text{C}$  data is shown in S8, ESI†). The reversible specific capacity for all four samples is above  $100\text{ mA h g}^{-1}$  on first discharge. This improvement in specific capacity over the  $500^\circ\text{C}$  annealed samples is most likely due to the improvement in crystallinity of the materials.

Fig. 6 shows typical electrochemical data from  $\text{Na}_2\text{CoSiO}_4$  produced with the NaCl flux agent present during the anneal. From the differential capacity plots, two clear redox events can be seen occurring. These events are further evidence for the presence of two distinct cobalt sites within the crystal structure. In contrast, the materials annealed without the NaCl flux agent (Fig. 5) show a more sloping voltage profile and broader differential capacity plot peaks. This is indicative of the cobalt in a shared crystallographic site with the silicon, which therefore gives a greater degree of solid-solution type behaviour. It is interesting to note that the voltage profile for  $\text{Na}_2\text{CoSiO}_4$  does not change from the first cycle to the second cycle, unlike that observed for the lithium analogues.<sup>11</sup> This indicates that sodium deintercalation and intercalation is fully reversible with no structural changes occurring in the fully sodiated orthosilicate.

The electrochemical performance of materials is linked not only to differences in the crystal structure of the compounds present but also to the morphological differences between samples.

The morphology of  $\text{Na}_2\text{CoSiO}_4$  synthesised by the co-precipitation method depends on both the annealing temperature and the presence of the NaCl flux agent. In order to illustrate how these factors change the resulting material, all the samples synthesised in this study were viewed using SEM.

At an annealing temperature of  $500^\circ\text{C}$ , both samples, regardless of the presence of NaCl during the anneal, appear to have primary particles of approximately  $200\text{--}300\text{ nm}$  in size that are roughly spherical. In both cases, these spherical particles are highly conjoined and appear to lack any substantial macroporosity (Fig. 7(a) and 8(a)).

At temperatures of  $700^\circ\text{C}$ , (Fig. 7(b) and 8(b)) differences due to the presence, or lack thereof, of the NaCl flux agent become more evident. Both samples at this temperature appear to consist of primary particles of approximately  $300\text{--}500\text{ nm}$  in size that have sintered to form a 3D network of secondary particles containing macropores. However, for the sample in which NaCl was present during the anneal, some of the primary particles can be seen to connect in a preferential direction leading to the creation of rod-like crystallites (Fig. 8(b)). It is this 3D porous network of small crystalline particles that exhibits the higher reversible capacities and a lowered hysteresis between charge and discharge compared to that found at  $500^\circ\text{C}$ .

At  $900^\circ\text{C}$ , a clear dependence in particle morphology on the presence of the NaCl flux agent can be observed. The sample without NaCl present during the anneal is highly sintered with large primary particles of approximately  $1\text{ }\mu\text{m}$  in diameter (Fig. 7(c)). The porosity between the primary particles has been



Fig. 7 SEM images of  $\text{Na}_2\text{CoSiO}_4$  with NaCl removed before annealing at (a) 500, (b) 700 and (c) 900 °C under flowing  $\text{N}_2$ .

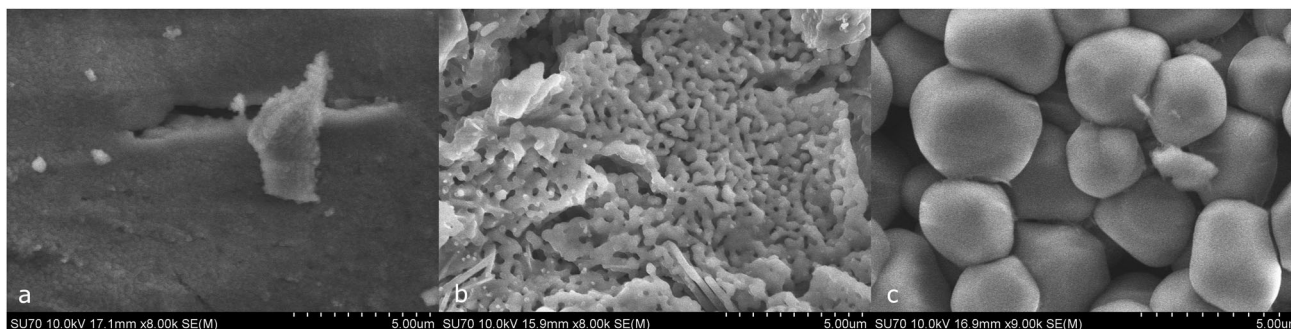


Fig. 8 SEM images of  $\text{Na}_2\text{CoSiO}_4$  annealed at (a) 500, (b) 700 and (c) 900 °C under flowing  $\text{N}_2$  in the presence of the NaCl flux agent (removed after).

removed and the primary particles are sintered into large dense agglomerates which lack macroporosity. In contrast, the sample in which the NaCl flux agent was present during the heat treatment appears to have a primary particle diameter of approximately 3  $\mu\text{m}$  (Fig. 8(c)) with these particles having a regular roughly spherical shape. The particles in this sample do not appear to be highly conjoined and therefore there is a large amount of space between them, resulting in the sample having a large porosity.

The sample heat-treated at 700 °C using NaCl as a flux agent represents the best morphology for further studies of  $\text{Na}_2\text{CoSiO}_4$  as a cathode material. This sample demonstrated the lowest hysteresis of all the samples tested, yielding a 0.08 V difference between charge and discharge on the second cycle. We believe that this result is likely due to the small primary particle size which minimises the ionic diffusion path length and the macroporous nature of the material, enabling good electrolyte penetration between the particles. The sample also demonstrated a good discharge capacity retention of 82% over 25 cycles. This will serve as a benchmark for further improvements through electrode formulation optimisation, tailoring of the electrolyte to the compound and use of the material with an anode other than Na metal. The early cycling efficiency is low, and this is in part due to the unoptimised electrolyte composition of 0.5 M  $\text{NaClO}_4$  in polycarbonate (PC) and the use of sodium metal counter electrode. It has been shown previously that there is instability of sodium metal in electrolyte solvents, and the efficiencies in these half-cell tests are always lower than those obtained in full cells due to the reaction of the sodium

metal, especially in PC solvent.<sup>47</sup> Other studies of electrolytes for sodium ion batteries show that there is room for improvement in this area, which is especially true for the silicate materials where no studies have yet been performed.<sup>47–49</sup>

It may be possible to have a two electron transfer in this  $\text{Na}_2\text{CoSiO}_4$  material if cycled to higher voltages. However, we observe faster fade rates in materials which are cycled to higher voltages (4.0–4.5 V vs.  $\text{Na}/\text{Na}^+$ ) and do not observe any more capacity. This is likely due to the structure collapse of the orthosilicate with more than one sodium removal from the structure, especially when cycled at room temperature. The cobalt orthosilicate materials are currently cycled to 3.75 V vs.  $\text{Na}/\text{Na}^+$  and a one electron process is observed, in which  $\text{Co}^{2+}$  is oxidised to  $\text{Co}^{3+}$  (eqn (1)). At the higher voltages required for  $\text{Co}^{3+} \rightarrow \text{Co}^{4+}$  in addition to the crystal structure collapse, there is an instability of the electrolyte solvents which may also contribute to the faster fading of the observed capacities.<sup>50</sup>



The performance of  $\text{Na}_2\text{CoSiO}_4$  when compared to the iron and the manganese analogues is very favourable. We have observed that  $\text{Na}_2\text{FeSiO}_4$  in particular is extremely sensitive to moisture due to the very low open circuit voltages and voltage plateaus (1.9 V vs.  $\text{Na}/\text{Na}^+$ ), but does deintercalate sodium at room temperature. The structure of  $\text{Na}_2\text{FeSiO}_4$  is also different to the  $\text{Na}_2\text{CoSiO}_4$  material and a single reversible sloping voltage curve is observed indicating a sodium solid solution ( $\text{S11}$ ,  $\text{ESI}^\dagger$ ). The manganese analogue exhibits extremely high polarisation and poor performance at room temperature. To date, as with

the lithium orthosilicates, most of the reported results for  $\text{Na}_2\text{MnSiO}_4$  have been obtained at temperatures greater than room temperature.<sup>18</sup>

### 3.3. Modelling of intrinsic defects and Na-ion diffusion

The defect chemistry and knowledge of the  $\text{Na}^+$  diffusion pathways in  $\text{Na}_2\text{CoSiO}_4$  are important to fully understand the electrochemical behaviour, which we examine here using atomistic simulation techniques. The starting point for the simulation work is the reproduction of the observed crystal structure. A comparison between the calculated structure based on the derived potentials (given in S9, ESI†) and experimental data for monoclinic  $Pn$  is shown in Table 2.

The structural reproduction is highly accurate with a maximum deviation of only 0.7% between the experimental and calculated unit cell parameters while the maximum bond length difference is 0.050 Å. The accurate reproduction of the experimental structure gives us confidence that the derived potentials can be used with accuracy in the defect and diffusion simulations.

A series of isolated point defect energies were calculated and combined to derive energies of formation for Frenkel and Schottky-type disorder. In addition, the Na/Co anti-site defect, involving the exchange of position of a pair of  $\text{Na}^+$  and  $\text{Co}^{2+}$  ions, was examined as it has been observed in other polyanionic systems such as  $\text{NaFePO}_4$  and  $\text{Li}_2\text{MnSiO}_4$ .<sup>35,51</sup> Representative example equations for these defects (in Kroger–Vink notation) are given in S9 (ESI†).

The defect formation energies are presented in Table 3 and two key points are raised. First, the high formation energies of all Frenkel and Schottky defects suggest that such intrinsic defects are unfavourable. Hence, such disorder is unlikely to be present in high concentrations in pristine  $\text{Na}_2\text{CoSiO}_4$ . Second, the lowest energy intrinsic defect is predicted to be the Na/Co anti-site defect. Similar disorder has been predicted to be favourable in other Na-ion cathode materials, such as  $\text{NaFePO}_4$  and  $\text{Na}_4\text{Fe}_3(\text{PO}_4)_2\text{P}_2\text{O}_7$ .<sup>35,43</sup> However, the magnitude of the anti-site formation energy is much higher than that typically found for other polyanionic cathode materials. For example, the corresponding anti-site energy is 0.86 eV for  $\text{NaFePO}_4$ .<sup>35</sup> These results suggest that the concentrations of intrinsic disorder in  $\text{Na}_2\text{CoSiO}_4$  are not significant. Hence, Na/Co anti-site defects would not be a major factor in blocking  $\text{Na}^+$  diffusion in this cathode material.

Table 2 Comparison between experimental and simulated unit cell parameters and mean bond lengths of  $Pn$   $\text{Na}_2\text{CoSiO}_4$

Parameter	Expt.	Calc.
$a$ (Å)	7.0433	7.0148
$b$ (Å)	10.9128	10.9452
$c$ (Å)	5.2396	5.2446
$\alpha$ (°)	90.00	90.00
$\beta$ (°)	90.02	89.88
$\gamma$ (°)	90.00	90.00
Na–O (Å)	2.358	2.322
Co–O (Å)	1.956	1.916
Si–O (Å)	1.621	1.670

Table 3 Calculated formation energies for intrinsic defects in  $\text{Na}_2\text{CoSiO}_4$

Defect	Energy (eV)
Na Frenkel	3.15
Co Frenkel	6.78
Si Frenkel	19.50
O Frenkel	8.88
Full Schottky	35.70
CoO Schottky-like	8.90
$\text{Na}_2\text{O}$ Schottky-like	10.86
$\text{SiO}_2$ Schottky-like	13.94
Na/Co anti-site	2.04

Sodium diffusion properties are of vital interest when considering the kinetics of electrode materials. MD simulations can be used to probe the energetics and topology of diffusion at the atomistic level. First, the mean square displacement (MSD),  $\langle [r(t)^2] \rangle$ , of  $\text{Na}^+$  ions was resolved, from which diffusion coefficients ( $D_{\text{Na}}$ ) were derived leading to a value of  $8.0 \times 10^{-12} \text{ cm}^2 \text{ s}^{-1}$  at 300 K. There is no experimental data for direct comparison. Nevertheless, the calculated diffusion coefficient is similar to those found in other Na-ion cathode materials, such as  $\text{Na}_x\text{MnO}_2$  ( $10^{-11} \text{ cm}^2 \text{ s}^{-1}$ ).<sup>52,53</sup>

The simulations were performed at several temperatures covering typical battery operating temperatures, and for a wider range than most diffusion experiments. Our diffusion coefficients can be used to estimate activation barriers from an Arrhenius plot ( $\ln(D)$  vs.  $1/T$ ), as shown in Fig. 9. A low migration activation barrier of 0.21 eV is predicted for  $\text{Na}_2\text{CoSiO}_4$ , indicative of fast bulk Na-ion transport and good electrode kinetics.

Diffusion trajectories can be visualised by plotting accumulated Na-ion densities, indicating the lattice sites most frequently traversed by  $\text{Na}^+$  ions during a simulation run. These are plotted in Fig. 10 and they clearly display a broad distribution and significant overlap of Na-ion density. This result confirms that  $\text{Na}^+$  ions are highly mobile, with all Na sites involved in bulk diffusion. Furthermore,  $\text{Na}^+$  diffusion can be seen to extend over a 3D network of migration pathways running throughout the silicate framework. This 3D isotropic behaviour is confirmed by the activation barriers for diffusion along the

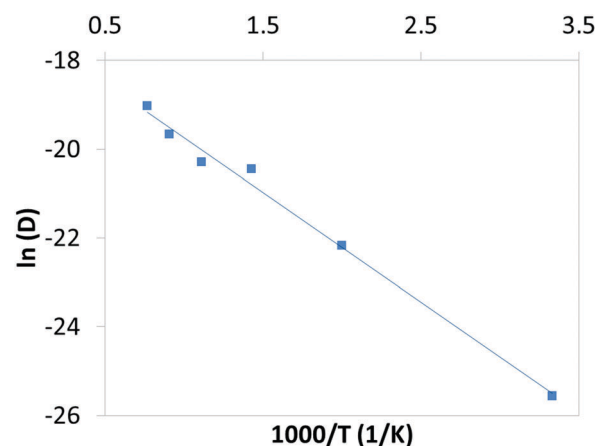


Fig. 9 Arrhenius plot of Na-ion diffusion coefficients vs. temperature ( $T$ ) derived from MD simulations of  $\text{Na}_2\text{CoSiO}_4$ .

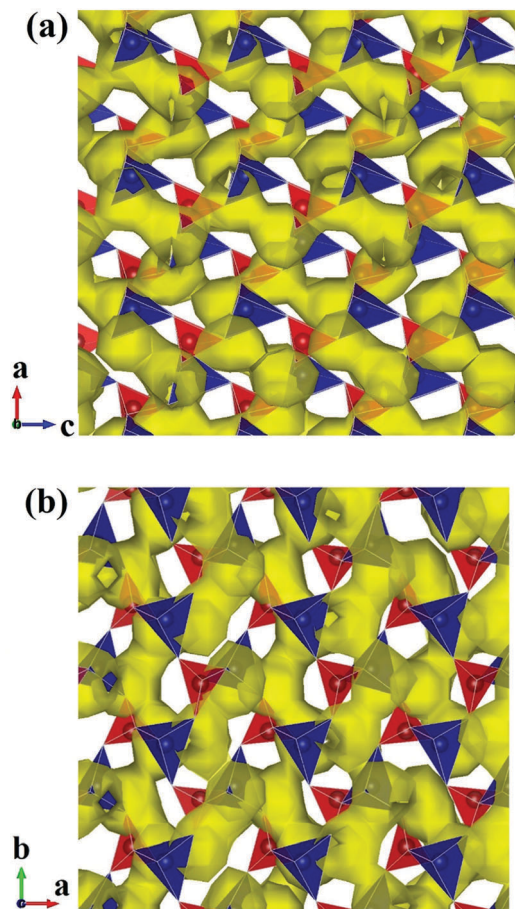


Fig. 10 Density plots of Na-ion diffusion pathways from MD simulations of  $\text{Na}_2\text{CoSiO}_4$  overlaid on initial lattice sites with two structural views: (a)  $ac$  plane and (b)  $ab$  plane. ( $\text{CoO}_4$  tetrahedra in blue,  $\text{SiO}_4$  tetrahedra in red and Na density in yellow).

$a$ ,  $b$  or  $c$  directions (S10, ESI<sup>†</sup>), which are found to be 0.21–0.22 eV. Closer analysis indicates that individual transitions between neighbouring Na sites take an essentially linear path, which is likely due to the open  $\text{SiO}_4$  framework that provides large migration windows between Na sites. Hence, Na-ion migration is relatively unhindered by  $\text{SiO}_4$  and  $\text{CoO}_4$  tetrahedra.

In short, the low activation barrier and 3D diffusion pathways are promising for good  $\text{Na}^+$  intercalation kinetics in  $\text{Na}_2\text{CoSiO}_4$  cathodes. These results contrast with the lithium silicate compounds,  $\text{Li}_2\text{MSiO}_4$  ( $M = \text{Mn, Fe or Co}$ ), which exhibit poor  $\text{Li}^+$  intercalation kinetics.

In order to improve the lithium orthosilicate electrochemical performances, testing of these materials are performed at higher temperatures, and the materials are nanosized and carbon coated. The work presented here shows the performance of a  $\text{Na}_2\text{CoSiO}_4$  at room temperatures with minimal carbon content. This reversible electrochemical intercalation at room temperature is an indication that the kinetics are improved in  $\text{Na}_2\text{CoSiO}_4$  over  $\text{Li}_2\text{CoSiO}_4$ . Ionic and electronic conductivities are both important parameters for rate performance. Although these sodium transition metal orthosilicates show improvements in performance due to the lower energy barriers to ionic diffusion, it is expected that

further optimisation is required to improve the electronic conductivities in these materials, similar to that which has been observed with the lithium analogues.

## 4. Conclusions

The crystal structures, electrochemistry and  $\text{Na}^+$  diffusion rates of the cathode material  $\text{Na}_2\text{CoSiO}_4$  have been investigated using a multi-technique approach. The following key results emerge:

(a)  $\text{Na}_2\text{CoSiO}_4$  was synthesised *via* a novel co-precipitation method. Two polymorphs, *Pn* and *Pbca*, were identified, both based upon a ‘stuffed’ cristobalite or the  $\beta\text{-NaFeO}_2$  type structure comprised of corner-sharing  $\text{SiO}_4$  and  $\text{CoO}_4$  tetrahedra with sodium filling the vacant tetrahedral sites. Without the NaCl flux agent, a disordered crystal structure is formed with Co and Si sharing the same crystallographic site, whereas with the flux agent, Si and Co are on distinct sites. At lower synthesis temperatures (700 °C), a 3D network of macroporous particles is observed.

(b) Electrochemical measurements using sodium metal anode cells demonstrate a reversible specific capacity on discharge of  $>100 \text{ mA h g}^{-1}$  for all samples synthesised at  $>500 \text{ °C}$ , with an average discharge voltage of 3.3 V vs.  $\text{Na/Na}^+$ . The structure of  $\text{Na}_2\text{CoSiO}_4$  does not change from the first cycle to the second cycle, in contrast with the lithium silicate analogues. Materials synthesised at 700 °C with the flux agent exhibited a lower hysteresis and good capacity retention due to the 3D network of macroporous particles.

(c) Atomic-scale simulations provide the first insights into the defect chemistry and  $\text{Na}^+$  diffusion pathways. The results suggest that the levels of intrinsic disorder in  $\text{Na}_2\text{CoSiO}_4$  are not significant and, in particular, Na/Co anti-site defects would not be a major factor in blocking  $\text{Na}^+$  diffusion in this cathode material. The MD simulations of  $\text{Na}^+$  diffusion indicate a very low activation barrier and a 3D network of diffusion pathways through the silicate framework, which suggest favourable  $\text{Na}^+$  intercalation kinetics.

The new insights into the structure, morphology and electrochemistry presented here provide a platform on which future optimisation of silicate cathodes for Na-ion batteries can be based.

## Acknowledgements

SMW thanks the EPSRC and the CDT in Sustainable Chemical Technologies for the PhD studentship. This work made use of HPC facilities *via* our membership of the Materials Chemistry Consortium, which is funded by EPSRC (EP/L000202). The authors thank J. A. Dawson (Bath) for useful discussions.

## References

- 1 B. L. Ellis and L. F. Nazar, *Curr. Opin. Solid State Mater. Sci.*, 2012, **16**, 168–177.
- 2 N. Yabuuchi, K. Kubota, M. Dahbi and S. Komaba, *Chem. Rev.*, 2014, **114**, 11636–11682.

- 3 V. Palomares, M. Casas-Cabanas, E. Castillo-Martínez, M. H. Han and T. Rojo, *Energy Environ. Sci.*, 2013, **6**, 2312–2337.
- 4 G. B. Haxel, J. B. Hedrick, G. J. Orris, P. H. Stauffer and J. W. Hendley II, *Rare earth elements: critical resources for high technology*, 2002.
- 5 H. Pan, Y.-S. Hu and L. Chen, *Energy Environ. Sci.*, 2013, **6**, 2338.
- 6 K. Kubota and S. Komaba, *J. Electrochem. Soc.*, 2015, **162**, A2538–A2550.
- 7 M. H. Han, E. Gonzalo, G. Singh and T. Rojo, *Energy Environ. Sci.*, 2014, **8**, 81–102.
- 8 C. Masquelier and L. Croguennec, *Chem. Rev.*, 2013, **113**, 6552–6591.
- 9 Z. Jian, L. Zhao, H. Pan, Y. S. Hu, H. Li, W. Chen and L. Chen, *Electrochem. Commun.*, 2012, **14**, 86–89.
- 10 A. Nytén, A. Abouimrane, M. Armand, T. Gustafsson and J. O. Thomas, *Electrochem. Commun.*, 2005, **7**, 156–160.
- 11 M. S. Islam, R. Dominko, C. Masquelier, C. Sirisopanaporn, A. R. Armstrong and P. G. Bruce, *J. Mater. Chem.*, 2011, **21**, 9811–9818.
- 12 R. Dominko, M. Bele, M. Gabersček, A. Meden, M. Remškar and J. Jamnik, *Electrochem. Commun.*, 2006, **8**, 217–222.
- 13 T. Muraliganth, K. R. Stroukoff and A. Manthiram, *Chem. Mater.*, 2010, **22**, 5754–5761.
- 14 S. Nishimura, S. Hayase, R. Kanno, M. Yashima, N. Nakayama and A. Yamada, *J. Am. Chem. Soc.*, 2008, **130**, 13212–13213.
- 15 D. Rangappa, K. D. Murukanahally, T. Tomai, A. Unemoto and I. Honma, *Nano Lett.*, 2012, **12**, 1146–1151.
- 16 R. J. Gummow and Y. He, *J. Power Sources*, 2014, **253**, 315–331.
- 17 H. Duncan, A. Kondamreddy, P. H. J. Mercier, Y. Le Page, Y. Abu-Lebdeh, M. Couillard, P. S. Whitfield and I. J. Davidson, *Chem. Mater.*, 2011, **23**, 5446–5456.
- 18 C.-Y. Chen, K. Matsumoto, T. Nohira and R. Hagiwara, *Electrochem. Commun.*, 2014, **45**, 63–66.
- 19 P. Zhang, Y. Xu, F. Zheng, S. Q. Wu, Y. Yang and Z.-Z. Zhu, *CrystEngComm*, 2015, **17**, 2123–2128.
- 20 Y. Kee, N. Dimov, A. Staykov and S. Okada, *Mater. Chem. Phys.*, 2016, DOI: 10.1038/srep15555.
- 21 X. Zhao, S. Wu, X. Lv, M. C. Nguyen, C.-Z. Wang, Z. Lin, Z.-Z. Zhu and K.-M. Ho, *Sci. Rep.*, 2015, **5**, 15555.
- 22 S. Li, J. Guo, Z. Ye, X. Zhao, S. Wu, J.-X. Mi, C.-Z. Wang, Z. Gong, M. J. McDonald, Z. Zhu, K.-M. Ho and Y. Yang, *ACS Appl. Mater. Interfaces*, 2016, **8**, 17233–17238.
- 23 L. Mu, S. Xu, Y. Li, Y. S. Hu, H. Li, L. Chen and X. Huang, *Adv. Mater.*, 2015, **27**, 6928–6933.
- 24 R. Von Dreele and A. Larson, *General structure analysis system (GSAS)*, 1994.
- 25 C. a Schneider, W. S. Rasband and K. W. Eliceiri, *Nat. Methods*, 2012, **9**, 671–675.
- 26 M. S. Islam and C. A. J. Fisher, *Chem. Soc. Rev.*, 2014, **43**, 185–204.
- 27 C. R. Catlow, *Computer Modelling in Inorganic Chemistry*, Academic Press, San Diego, 1997.
- 28 C. R. Catlow, *Computational Approaches to Energy Materials*, Wiley, Chichester, UK, 2013.
- 29 J. D. Gale, *J. Chem. Soc., Faraday Trans.*, 1997, **93**, 629–637.
- 30 M. S. Islam, D. J. Driscoll, C. A. J. Fisher and P. R. Slater, *Chem. Mater.*, 2005, **17**, 5085–5092.
- 31 J. M. Clark, S. Nishimura, A. Yamada and M. S. Islam, *Angew. Chem., Int. Ed.*, 2012, **51**, 13149–13153.
- 32 A. R. Armstrong, C. Lyness, P. M. Panchmatia, M. S. Islam and P. G. Bruce, *Nat. Mater.*, 2011, **10**, 223–229.
- 33 Y. G. Andreev, P. M. Panchmatia, Z. Liu, S. C. Parker, M. S. Islam and P. G. Bruce, *J. Am. Chem. Soc.*, 2014, **136**, 6306–6312.
- 34 J. M. Clark, P. Barpanda, A. Yamada and M. S. Islam, *J. Mater. Chem. A*, 2014, **2**, 11807–11812.
- 35 R. Tripathi, S. M. Wood, M. S. Islam and L. F. Nazar, *Energy Environ. Sci.*, 2013, **6**, 2257–2264.
- 36 S. Plimpton, *J. Comput. Phys.*, 1995, **117**, 1–19.
- 37 A. Pedone, G. Malavasi, M. C. Menziani, A. N. Cormack and U. Segre, *J. Phys. Chem. B*, 2006, **110**, 11780–11795.
- 38 C. Tealdi, C. Spreafico and P. Mustarelli, *J. Mater. Chem.*, 2012, **22**, 24870–24876.
- 39 M. Salanne, D. Marrocchelli and G. W. Watson, *J. Phys. Chem. C*, 2012, **116**, 18618–18625.
- 40 P. M. Panchmatia, A. Orera, G. J. Rees, M. E. Smith, J. V. Hanna, P. R. Slater and M. S. Islam, *Angew. Chem.*, 2011, **123**, 9500–9505.
- 41 P. M. Panchmatia, A. R. Armstrong, P. G. Bruce and M. S. Islam, *Phys. Chem. Chem. Phys.*, 2014, **16**, 21114–21118.
- 42 A. R. Armstrong, N. Kuganathan, M. S. Islam and P. G. Bruce, *J. Am. Chem. Soc.*, 2011, **133**, 13031–13035.
- 43 S. M. Wood, C. Eames, E. Kendrick and M. S. Islam, *J. Phys. Chem. C*, 2015, **119**, 15935–15941.
- 44 W. H. Baur, T. Ohta and R. D. Shannon, *Acta Crystallogr., Sect. B: Struct. Crystallogr. Cryst. Chem.*, 1981, **37**, 1483–1491.
- 45 C. A. Joubert-Bettan, R. Lachenal, E. F. Bertaut and E. Parthé, *J. Solid State Chem.*, 1969, **1**, 1–5.
- 46 L. Bao, W. Gao, Y. Su, Z. Wang, N. Li, S. Chen and F. Wu, *Chin. Sci. Bull.*, 2012, **58**, 575–584.
- 47 A. Ponrouch, E. Marchante, M. Courty, J.-M. Tarascon and M. R. Palacin, *Energy Environ. Sci.*, 2012, **5**, 8572–8583.
- 48 A. Ponrouch, D. Monti, A. Boschini, B. Steen, P. Johansson and M. R. Palacin, *J. Mater. Chem. A*, 2015, **3**, 22–42.
- 49 K. Vignarooban, R. Kushagra, A. Elango, P. Badami, B. E. Mellander, X. Xu, T. G. Tucker, C. Nam and A. M. Kannan, *Int. J. Hydrogen Energy*, 2016, **41**, 2829–2846.
- 50 S. Komaba, T. Ishikawa, N. Yabuuchi, W. Murata, A. Ito and Y. Ohsawa, *ACS Appl. Mater. Interfaces*, 2011, **3**, 4165–4168.
- 51 N. Kuganathan and M. S. Islam, *Chem. Mater.*, 2009, **21**, 5196–5202.
- 52 T. Shibata, W. Kobayashi and Y. Moritomo, *Appl. Phys. Express*, 2014, **7**, 67101.
- 53 T. Jiang, G. Chen, A. Li, C. Wang and Y. Wei, *J. Alloys Compd.*, 2009, **478**, 604–607.